Numerical Simulation of Discrete Wind Gusts Generated by an Adaptive Nozzle Using a Dynamic Immersed Boundary Method

Khaled Boulbrachene and Michael Breuer

Abstract A wind gust is a short-term but strong phenomenon naturally appearing in the atmospheric boundary layer. Fluid-structure interaction investigations under wind gust conditions, ideally in a wind tunnel with controlled parameters, are essential for evaluating the safety of final designs for example in civil engineering. For this purpose, Wood et al. (J Wind Eng Ind Aerodyn 230:105170, 2022) developed a novel wind gust generator denoted the "Paddle". Its basic principle relies on the partial dynamic blocking of the wind tunnel nozzle's outlet by a vertically moving plate that penetrates the free-stream. The setup and the flow induced by the paddle were numerically simulated in Boulbrachene and Breuer (Phys Fluids 36:015146, 2024) by employing an immersed boundary method (IBM) relying on a direct forcing approach to mimic the motion of the paddle. This configuration restricted the undisturbed gust region in the test section of the wind tunnel as a result of the shear layer forming at the lower edge of the moving paddle. Moreover, it caused an undershoot of the gust velocity below the free-stream velocity as a result of high pressure losses associated with the paddle's blockage effect. Wood and Breuer (Artificial wind gust generation based on an adaptive nozzle design. Berlin, pp 9-1–9-8, 2024) and Wood and Breuer (J Wind Eng Ind Aerodyn 261:106080, 2025) recently introduced an improved design that addresses the shortcomings of the paddle while maintaining the same underlying principle for generating the gust. The new setup features an adjustable nozzle with a fully rotatable upper contour to generate smoother wind gusts. In order to gain a comprehensive understanding of the evolving flow field during the movement of the nozzle's upper boundary, large-eddy simulations of the process are conducted. This involves modeling the nozzle's upper boundary as a moving immersed boundary using again the IBM with direct forcing but this time on a curvilinear Eulerian grid. The numerical methodology and its application to the movable nozzle case is presented in the present study. The predicted results are analyzed in detail and compared with available experimental measurement data (Wood and

K. Boulbrachene · M. Breuer (✉)
Professur für Strömungsmechanik, Helmut-Schmidt-Universität Hamburg, Hamburg, Germany
e-mail: breuer@hsu-hh.de

K. Boulbrachene
e-mail: boulbrak@hsu-hh.de

M. Schäfer et al. (eds.), *New Trends in Computational Engineering*,
Lecture Notes in Computational Science and Engineering 150,
https://doi.org/10.1007/978-3-032-16253-3_3

Breuer in Artificial wind gust generation based on an adaptive nozzle design. Berlin, pp 9-1–9-8, 2024) and (Wood and Breuer in J Wind Eng Ind Aerodyn 261:106080, 2025).

1 Introduction

The study investigates an adaptive nozzle concept designed for the generation of artificial wind gusts in a wind tunnel and validated through the experimental measurements of Wood and Breuer [12, 13]. The experiments were conducted in an Eiffel-type wind tunnel featuring key components such as a blower, diffusor, settling chamber with honeycomb straighteners, and an adaptive nozzle with a movable upper contour, see Fig. 1. The nozzle, with a contraction ratio of 2:1, initially possesses an outlet cross-section of 0.25 m × 0.5 m. The gust generator operates by dynamically reducing the nozzle's outlet area, thereby increasing the velocity according to the principle of mass conservation. Rapid area reductions cause sharp velocity increases, mimicking wind gusts as they occur in nature. An earlier paddle-based design [11, 14] validated this principle but suffered from strong pressure losses and severe shear layers caused by flow separation at the paddle.

The second-generation gust generator attenuates these issues using a movable upper contour of the nozzle as sketched in Fig. 1. A servo-driven tooth belt axis, which performs a vertical downwards and upwards motion, leads to the rotation of the upper nozzle's contour around a rotatable bearing. The kinematic characteristics of the motion pattern provided in Sect. 4 can be fully controlled via an automation software tool.

Since the concept of the experimental gust generator is based on the nozzle with a movable upper contour, this particular feature must be incorporated into the numerical flow simulation. One possible approach is the Arbitrary Lagrangian-Eulerian

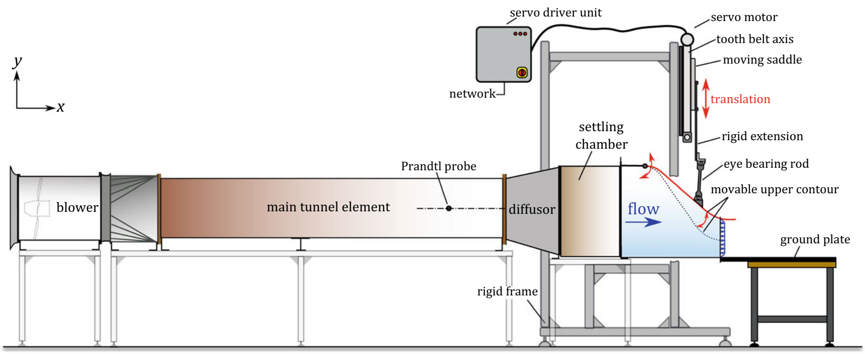

Fig. 1 Sketch of the Eiffel-type wind tunnel with the adaptive nozzle contour in red (Two sketches from [13] merged)

(ALE) method, where the fluid mesh conforms to the geometry of the upper contour, and the no-slip boundary condition is enforced on the surface of the nozzle defining the fluid-structure interaction (FSI) interface at each time step. While the ALE method excels at accurately resolving the flow along the fluid-structure interface, it suffers from significant drawbacks in FSI problems with large displacements. These drawbacks include the need for a time-consuming grid adaptation [7] during the simulation, which significantly increases computational costs. Additionally, heavily adapted grids may suffer from poor grid quality (orthogonality and smoothness), potentially compromising the accuracy of the numerical results.

An alternative is the immersed boundary method (IBM) originally introduced by Peskin [5], relying on overlapping discretizations for the fluid and structural domains. The no-slip boundary condition is enforced on the fluid-solid interface by formulating an appropriate boundary forcing term. Among the various IBM categories proposed in the literature (see, e.g., Mittal and Iaccarino [4]), the continuous forcing IBM (diffuse-interface immersed boundary) with the direct forcing approach of Uhlmann [9] is employed in the present study due to its convenience for moving immersed boundaries. In the direct forcing IBM, boundary forces are computed on the Lagrangian markers (rather than the Eulerian grid points) before being smeared over a few Eulerian cells in their vicinity by means of a regularized delta function kernel. This approach results in smoother hydrodynamic forces.

To improve the computational performance of the simulations carried out in this work, the Lagrangian markers are placed within a non-uniform curvilinear Eulerian grid, clustering points within the range of motion of the upper contour. Consequently, Eulerian grid points are distributed non-uniformly around the Lagrangian markers. The direct use of IBM kernels derived for uniform grids would violate the integral conservation of force and moment. Therefore, the moving least squares (MLS) version of the direct forcing IBM introduced by Vanella and Balaras [10] is employed. The MLS methodology constructs interpolation kernels for each Lagrangian marker by solving a weighted least squares problem defined over a set of its neighboring Eulerian points, accommodating their non-uniform distribution. The interpolation kernel generated by the MLS construction satisfies the polynomial reproduction constraints, ensuring the integral conservation of force and moment.

2 Computational Framework

2.1 Numerical Basis

The present study employs the in-house FASTEST-3D [3] Navier-Stokes solver for incompressible flow simulations. The governing equations are discretized using the finite-volume method on a curvilinear, block-structured grid with a collocated cell-centered variable arrangement. Domain decomposition and MPI-based message passing enable parallelization. The spatial accuracy is second-order, achieved by using the midpoint rule approximation for the surface and volume integrals. The flux blending technique, combining 3 % of a first-order upwind scheme with 97 % of a second-order central scheme, is used for approximating the convective fluxes. The Rhie and Chow momentum interpolation technique [6] couples the pressure and velocity fields, ensuring stability and preventing oscillations on non-staggered grids.

A semi-implicit predictor-corrector scheme [2] is employed for the pressure-velocity coupling problem. Initially, the momentum equations are advanced in time using a multi-stage Runge-Kutta method to obtain an intermediate velocity. The direct forcing IBM (detailed in Sect. 2.2) incorporates the effect of the immersed boundary representing the structure on the fluid in three steps. First, the intermediate velocity at the discrete Lagrangian locations (i.e., Lagrangian markers) is evaluated. Then, the fluid-solid boundary force is determined based on the difference between the desired and the interpolated velocity at the Lagrangian markers. Finally, the force is spread from the Lagrangian markers to their neighboring Eulerian cells as a volume force that is used to evaluate a second intermediate velocity. This second intermediate velocity satisfies the no-slip boundary condition at the fluid-solid interface. The predictor-corrector method finally proceeds by solving the Poisson equation for the pressure correction, ensuring that the flow fields are projected into a divergence-free vector space. Overall, this approach ensures second-order accuracy in space and time.

Large-eddy simulations (LES) resolve large-scale turbulence while modeling small scales using the classic Smagorinsky [8] subgrid-scale model with $C_s = 0.1$ and van-Driest damping near solid walls. With sufficient near-wall grid resolution, wall-resolved LES is performed without wall functions.

2.2 *Immersed Boundary Method With Direct Forcing*

The direct forcing IBM evaluates the force at the fluid-solid interface within the Lagrangian frame of reference. The force is defined such that the no-slip boundary condition is enforced at each Lagrangian marker l. Within the context of the predictor-corrector scheme, the Lagrangian volume force at a time step t^n is given by Uhlmann [9]:

$$\mathbf{F}_l^n = \rho \, \frac{\mathbf{U}_l^d - \mathbf{U}_l^*}{\Delta t} \; . \tag{1}$$

Here, $\mathbf{U}_l^d$ and $\mathbf{U}_l^*$ represent the desired and the intermediate velocity at the Lagrangian location $\mathbf{X}_l$, respectively. The desired velocity $\mathbf{U}_l^d$ is defined by the rigid-body motion of the nozzle's upper contour, as described in Sect. 3. Since the Lagrangian markers are generally not coinciding with the Eulerian grid points, the intermediate velocity $\mathbf{U}_l^*$ at the location of the Lagrangian marker is obtained by an interpolation operation, evaluating a discrete Lagrangian velocity as a weighted average of neighboring discrete Eulerian velocities:

$$\mathbf{U}_l^* = \sum_{e \in N_{E,l}} \mathbf{u}_e^* \, \phi_{e,l} \ , \tag{2}$$

where $N_{E,l}$ denotes the set of Eulerian cells, whose centroids lie within the support of the kernel associated with the lth Lagrangian marker, and $\phi_{e,l}$ is the discrete interpolation weight of the eth Eulerian cell that reads:

$$\phi_{e,l} = \varphi \left(\mathbf{x}_e - \mathbf{X}_l \right) \, \Delta v_e \ , \tag{3}$$

where $\varphi \left(\mathbf{x}_e - \mathbf{X}_l \right)$ is the tensor product of the kernel function normalized by the dilation parameter, and Δv_e is the volume of the eth Eulerian cell. After evaluating the intermediate velocity at the Lagrangian locations, Eq. (1) is employed to compute the volume force at the fluid-solid interface. The impact of the immersed boundary on the surrounding fluid is incorporated into the discrete governing equations by the spreading operation evaluating the Eulerian volume force as:

$$\mathbf{f}_e = \sum_{l \in N_{L,e}} \mathbf{F}_l \, \phi_{e,l} \, \frac{\Delta V_l}{\Delta v_e} = \sum_{l \in N_{L,e}} \mathbf{F}_l \, \phi_{e,l} \, W_l \ . \tag{4}$$

Here, $N_{L,e}$ represents the set of Lagrangian markers, whose kernel support includes the eth Eulerian cell, while ΔV_l and W_l denote the volume and the spreading weight associated to the lth Lagrangian marker, respectively. It is desired for the discrete interpolation weights to satisfy the discrete zeroth and first moment conditions:

$$\sum_{e \in N_{E,l}} \phi_{e,l} = 1 \qquad \forall \, l \ , \tag{5}$$

$$\sum_{e \in N_{E,l}} \left(\mathbf{x}_e - \mathbf{X}_l \right) \, \phi_{e,l} = 0 \qquad \forall \, l \ . \tag{6}$$

These conditions guarantee the integral conservation of force and torque in the spreading operation. On uniform grids, these conditions are automatically satisfied if the chosen kernel φ is designed to inherently possess the desired properties (e.g., Peskin's kernel functions [5]).

In contrast to most IBM applications, this study employs a curvilinear stretched grid to discretize the nozzle region (as depicted in Fig. 3 and explained in Sect. 3). Thus, this work adopts the moving least squares version of the direct forcing immersed boundary method (MLS-IBM) introduced by Vanella and Balaras [10]. The moving least square approximation interpolates the kth Eulerian velocity component u^k from a set of arbitrarily distributed neighboring Eulerian points to the discrete location of the lth Lagrangian marker by:

$$U_l^k = \sum_{i=1}^{m} p_i(\mathbf{X}_l)\, a_i(\mathbf{X}_l) = \mathbf{p}(\mathbf{X}_l)^\mathsf{T}\, \mathbf{a}(\mathbf{X}_l) \ . \tag{7}$$

Here, $\mathbf{p} \in \mathbb{R}^m$ is the basis function vector and $\mathbf{a} \in \mathbb{R}^m$ is the vector of unknown coefficients. For a second-order accurate three-dimensional spatial discretization scheme, it is sufficient and cost efficient to define $\mathbf{p}$ as a linear basis function vector (i.e., $m = 4$ and $\mathbf{p}(\mathbf{x}) = [1 \quad x \quad y \quad z]$). The unknown coefficient vector $\mathbf{a}(\mathbf{X}_l)$ is found by minimizing the weighted L^2-norm of the error function:

$$\min_{\mathbf{a}(\mathbf{X}_l)} \quad J_l = \frac{1}{2} \left(\mathcal{A}^\mathsf{T}\, \mathbf{a}(\mathbf{X}_l) - \mathbf{u}^k\right)^\mathsf{T} \operatorname{diag}(\boldsymbol{\phi}_l) \left(\mathcal{A}^\mathsf{T}\, \mathbf{a}(\mathbf{X}_l) - \mathbf{u}^k\right) \ , \tag{8}$$

where $\mathbf{u}^k \in \mathbb{R}^{N_{E,l}}$, $\boldsymbol{\phi}_l \in \mathbb{R}^{N_{E,l}}$ is the vector of interpolation weights, and the entries of the polynomial matrix $\mathcal{A} \in \mathbb{R}^{m \times N_{E,l}}$ are the values of the basis functions at the Eulerian interpolation stencil (i.e., $\mathcal{A}_{ij} = p_i(\mathbf{x}_j)$, with $i = 1, ..., m$, $j = 1, ..., N_{E,l}$). Minimizing the error J_l with respect to the vector of unknown coefficients yields:

$$\mathbf{a}(\mathbf{X}_l) = \mathcal{G}^{-1}\, \mathcal{B}\, \mathbf{u}^k \ , \tag{9}$$

where $\mathcal{G} = \mathcal{A} \operatorname{diag}(\boldsymbol{\phi}_l)\, \mathcal{A}^\mathsf{T} \ \in \mathbb{R}^{m \times m}$ is the positive-definite Gram matrix and $\mathcal{B} = \mathcal{A} \operatorname{diag}(\boldsymbol{\phi}_l) \ \in \mathbb{R}^{m \times N_{E,l}}$. Hence, Eq. (7) simplifies to:

$$U_l^k = \mathbf{p}(\mathbf{X}_l)^\mathsf{T}\, \mathcal{G}^{-1}\, \mathcal{B}\, \mathbf{u}^k = \tilde{\boldsymbol{\phi}}_l^\mathsf{T}\, \mathbf{u}^k = \sum_{e \in N_{E,l}} \tilde{\phi}_{e,l}\, u_e^k \ . \tag{10}$$

The modified interpolation weights ($\tilde{\phi}_{e,l}$) obtained from the MLS solution satisfy the discrete moment conditions in Eqs. (5) and (6). For further details, refer to [10].

3 ComputationaL Setup

This work focuses on modeling the wind gust generator, particularly the adaptive nozzle, as described in [12, 13]. The computational approach provides insights into the flow characteristics by predicting velocity and pressure distributions within the entire computational domain and over the entire gust generation process. The setup, shown in Fig. 2, mimics the experimental arrangement in Fig. 1. At the inlet, air enters with a uniform velocity of $u_{\text{inlet}}^{\text{steady}} = 2.54\,\text{m/s}$. Boundary layers form along the duct and nozzle walls, reaching a velocity of $u_\infty = 5.14\,\text{m/s}$ in the core area of the outlet, consistent with the experimental conditions. An additional temporal adjustment of the inlet velocity is explained below.

No-slip and impermeability constraints are applied to all wall boundaries, while a convective boundary condition is used at the outlet with the convection velocity set to $u_{\text{conv}} = u_\infty$. To simplify the upstream section, a square duct with a 1 m length and

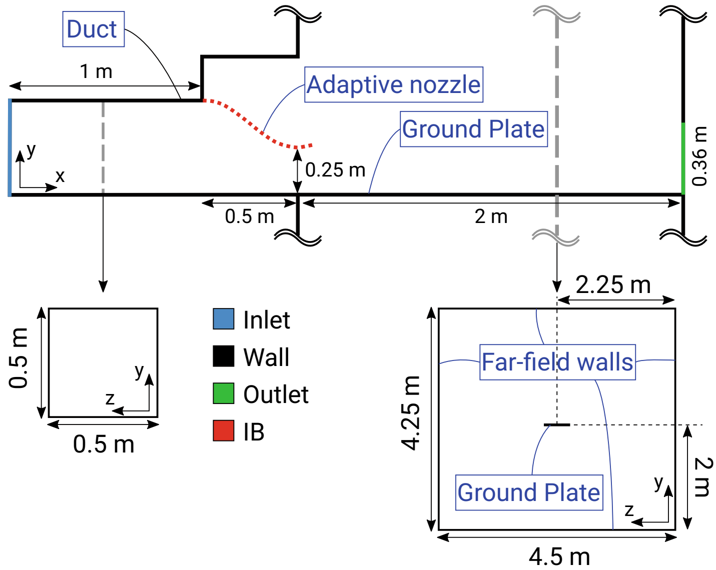

Fig. 2 Geometry of the test case and boundary conditions

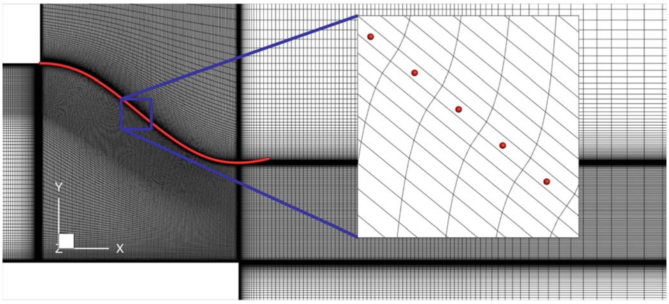

Fig. 3 Detailed view of the computational grid near the nozzle's contour in the x-y symmetry plane. Every second grid line in each direction is displayed. The zoomed-in view shows the distribution of the Lagrangian markers (red spheres) within the curvilinear grid

an edge length of $w = 0.5$ m replaces components such as the diffuser and the flow straightener. The nozzle retains its original 2:1 contraction ratio, ensuring boundary conditions aligned with the experimental setup.

The computational grid, partially shown in Fig. 3, is a block-structured curvilinear mesh consisting of 105.6×10^6 control volumes. Initially defined with 12 blocks, the grid has been further subdivided into 786 parallel blocks. This partitioning facilitates parallel computations across 786 cores, achieving a load balancing efficiency of 100 % when running pure CFD simulations without incorporating Lagrangian markers.

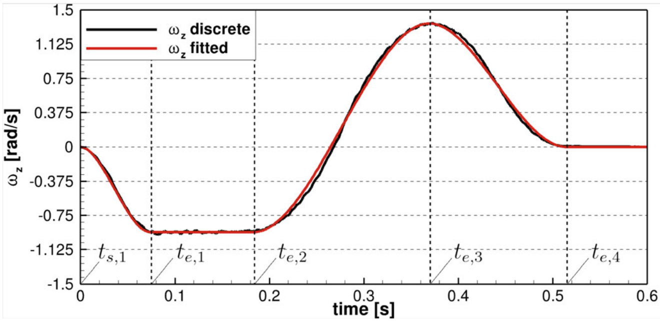

Fig. 4 Kinematic characteristics of the fitted rotational velocity

To resolve the pronounced viscous effects responsible for the formation of thin boundary layers, the grid is refined near rigid surfaces, including the duct and nozzle walls, as well as the ground plate. This ensures that the centers of the first grid cells are within the viscous sublayer ($y^+ < 5$).

The upper contour of the nozzle, modeled as an immersed boundary, is represented by a set of Lagrangian markers. The distribution of the Lagrangian markers is designed to prevent fluid from penetrating through the fluid-solid interface. This issue arises when the Lagrangian grid is too coarse relative to the Eulerian grid, resulting in inadequate coverage of Eulerian cells by the Lagrangian marker window function. Therefore, markers are distributed such that their local spacing is equal to or less than the local Eulerian grid resolution encountered during the nozzle's motion.

The rotational motion of the nozzle's upper contour is derived from the saddle's prescribed vertical motion. This translational-to-rotational motion conversion is facilitated by an eye-bearing rod. The experimentally defined time-dependent vertical displacement and velocity of the saddle are used to compute a discrete rotational velocity $\omega_z(t)$. A smooth analytical function is then fitted to this rotational velocity as depicted in Fig. 4. The resulting fitted function for $\omega_z(t)$ is given by:

$$\omega_{z,\text{fit}}(t) = \begin{cases} -A_1\left(3\phi_1^2 - 2\phi_1^3\right), & \text{if } t_{s,1} = 0\,\text{s} \le t < t_{e,1} = 0.075\,\text{s} \\ -A_1, & \text{if } t_{s,2} = t_{e,1} \le t < t_{e,2} = 0.184\,\text{s} \\ A_2\left(3\phi_3^2 - 2\phi_3^3\right) - A_1, & \text{if } t_{s,3} = t_{e,2} \le t < t_{e,3} = 0.37\,\text{s} \\ (A_2 - A_1) - (A_2 - A_1)\left(3\phi_4^2 - 2\phi_4^3\right), & \text{if } t_{s,4} = t_{e,3} \le t < t_{e,4} = 0.515\,\text{s} \\ 0, & \text{otherwise,} \end{cases} \tag{11}$$

where $\phi_i = \left(t - t_{mid,i}\right)/t_{w,i}, t_{mid,i} = \left(t_{e,i} + t_{s,i}\right)/2, t_{w,i} = t_{e,i} - t_{s,i}, A_1 = 0.934\,\text{m/s}$, and $A_2 = 2.284$ m/s.

The translational velocities of each Lagrangian force point are then evaluated by:

$$\mathbf{U}_l^d(\mathbf{X}_l) = \boldsymbol{\omega}_{\text{fit}} \times (\mathbf{X}_l - \mathbf{x}_c)\,, \tag{12}$$

where $\mathbf{x}_c$ is the center of rotation of the immersed boundary and $\boldsymbol{\omega}_{\text{fit}} = \left[0,\ 0,\ \omega_{z,\text{fit}}\right]$. As visible in Fig. 4, the entire gust generation time is presently set to $\Delta t_{\text{gust}} = 0.5$ s. This characteristic time scale is also used in Sect. 4 to normalize the time axis.

In the experiments carried out by Wood and Breuer [13], an undershoot of the streamwise velocity below the free-stream velocity was observed at the nozzle's outlet in the wake of the generated gust. The authors attributed this phenomenon to pressure losses caused by the sudden partial closure of the adaptive nozzle. This was confirmed by placing a Prandtl probe inside the main tunnel element (see Fig. 1) during the gust generation and calculating the dynamic pressure as the difference between the measured total and static pressures. Based on this dynamic pressure, the reduction in the inlet velocity was determined. To replicate this undershooting in the simulation, a similar time-dependent inlet boundary condition is defined.

4 Results and Discussion

The analysis focuses on illustrating the time-dependent flow characteristics of the gust generated by the rotational motion of the nozzle's upper contour. Figure 6 shows the streamwise velocity component and the pressure distribution in the x-y symmetry plane at five distinct instants in time annotated in Fig. 5. The monitoring points, labeled 1 to 9, mark specific positions in the test section of the wind tunnel selected for comparison with the experimental data [12, 13]. These positions correspond to the region where a wind tunnel model is typically placed.

At instant 1 (i.e., at $t/\Delta t_{\text{gust}} \approx 0$), the nozzle's upper contour is in its idle position, and the flow fields represent the initial conditions for the numerical gust generator. In this state, the flow is allowed to fully develop, with the immersed boundary remaining stationary to establish a stable reference condition before any dynamic motion begins. Two distinct flow phenomena are visible at this stage. First, boundary layers form along the top and bottom walls of the nozzle, with the development continuing along the ground plate for the latter. Second, a free shear layer develops in the region, separating the high-velocity core flow from the surrounding slower-moving fluid.

At instant 2 (i.e., at $t/\Delta t_{\text{gust}} \approx 0.25$), the nozzle's upper contour moves downward from its idle position, partially obstructing 17 % of the nozzle's original outlet area. This reduction in area causes the streamwise velocity to increase above the ground plate. However, unlike the flow situation induced by the paddle gust generator, the flow exiting the nozzle maintains its original path, demonstrating one of the advantages of the new design. It can also be observed that the movement of the upper contour leads to an increase in the static pressure inside the nozzle. Furthermore, the formation of a small vortex near the tip of the nozzle's upper contour is seen.

At instant 3 (i.e., at $t/\Delta t_{\text{gust}} \approx 0.5$), the upper contour's downstroke is completed and the maximum blocking ratio of 36.7 % is reached. The highest streamwise velocity values extending along the ground plate are recorded, characterizing the strong horizontal wind gust generated. The initially thick free shear layer observed near the tip of the upper contour at instant 1 has become sharper, dynamically adjusting

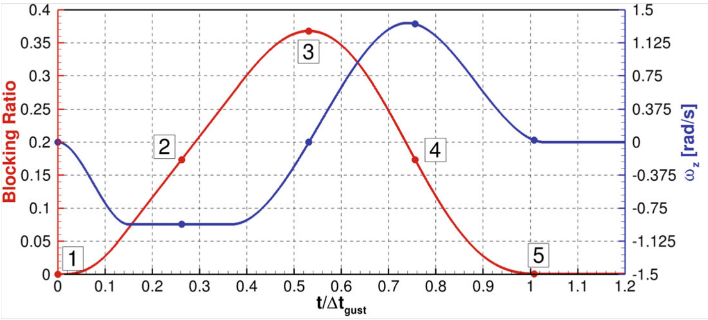

Fig. 5 Nozzle's blocking ratio annotated with five characteristic time instants at which the flow is visualized in Fig. 6; upper rotational velocity of the contour during the downward and upward strokes

its altitude to follow the contour's motion. In contrast to the streamwise velocity, lower pressure values are recorded inside the nozzle compared to those at instant 2. This reduction results from the lower velocity values prescribed at the inlet patch, accounting for the wind tunnel's reduced airflow caused by the sudden increase in the blocking ratio. Nevertheless, a strong pressure gradient persists, continuing to accelerate the flow beneath the nozzle's upper contour. The vortical structure, formed due to the interaction between the moving contour's tip and the flow, has grown in size and is convected further downstream.

Instant 4 (i.e., $t/\Delta t_{\mathrm{gust}} \approx 0.75$) captures the upward return of the contour toward its idle position. During this phase, the strength of the generated gust already decreases as the flow expands within the outlet. Simultaneously, the free shear layer is destabilized as small vortices are shed from the upper contour's tip resulting in a streamwise velocity field with turbulent characteristics. Moreover, the free shear layer becomes inclined (no longer horizontal) as it is unable to adjust quickly enough to the rapid upward movement of the nozzle's contour.

At instant 5 (i.e., at $t/\Delta t_{\mathrm{gust}} \approx 1$), the nozzle's upper contour is back to its idle position and the flow gradually recovers toward its initial state.

A preliminary comparison between the predicted data and the Constant Temperature Anemometry (CTA) measurements by Wood and Breuer [12, 13] is shown in Fig. 7. The comparison is based on the time histories of the velocity magnitude at the aforementioned 9 monitoring points in Fig. 6a. Phase-averaging of the velocity magnitude was performed in the experiments [12, 13] based on 46 gust events. The need for phase-averaging arises due to the presence of the turbulent free shear layer at the top surface of the jet exiting the nozzle [1]. At this shear layer, small vortices are formed and convected downstream, as shown for instant 1 in Fig. 6b, making the flow generated by the upper contour's motion dependent on the flow state at the onset of movement. Nevertheless, the numerical results derived from a single gust event are chosen here for comparison to emphasize the instantaneous flow behavior.

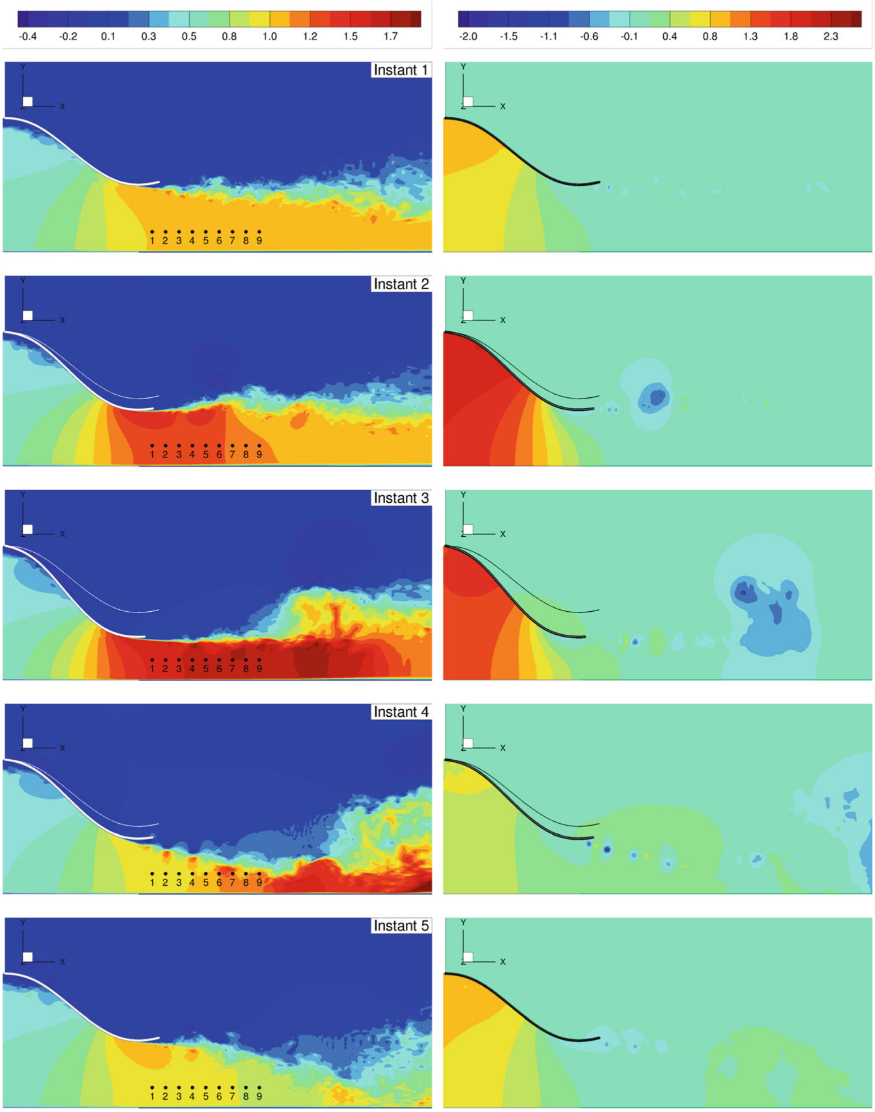

(a) u/u_∞ (b) $p/(0.5\rho u_\infty^2)$

Fig. 6 Snapshots of the streamwise velocity (**a**) and the pressure (**b**) during the downward and upward strokes of the nozzle's upper contour. Instants correspond to those depicted in Fig. 5. For the instants 2 to 4, a line indicating the upper contour's idle position is depicted for reference

Overall, the time histories at single monitoring points exhibit a bell-shaped pattern, which is consistent with the blocking ratio curve of the nozzle. According to the principle of mass conservation, the flow beneath the upper contour is forced to accelerate as the nozzle's outlet undergoes further contraction. This acceleration continues until the maximum blocking ratio is reached. As the contour returns to its idle position, the streamwise velocity decelerates. The subsequent drop below the free-stream velocity results at least partially from the prescribed transient inlet velocity, which models the reduced airflow through the wind tunnel's blower. This velocity undershoot becomes more pronounced as the gust is convected downstream.

The velocity magnitude curves for the monitoring points 1 to 3 (i.e., Fig. 7a–c) closely align with those observed in the experimental data. However, for the monitoring points 4 to 9 (i.e., Fig. 7d–i), the descending slopes of these curves exhibit an increasingly chaotic and turbulent behavior, becoming more pronounced as one moves downstream. Obviously, these fluctuations are filtered out in the phase-averaged experimental data. However, in the instantaneous data of Wood and Breuer [12, 13] (not shown here) oscillations of the velocity magnitude comparable to those found in the LES predictions were observed. These fluctuations are attributed to the separation of the turbulent flow occurring near the tip of the nozzle's upper contour due to its fast upward movement. This separation generates a series of small vortices, destabilizing the inclined shear layer and interfering with the flow at the monitoring points downstream, as shown at instant 4 in Fig. 6a.

A distinct feature in the velocity signals worth highlighting are the velocity peaks. During the gust generation period (i.e., for $t/\Delta t_{\text{gust}} \leq 1$), a dent is formed in the peak of the velocity signal at the fifth's streamwise location (see Fig. 7e). This feature then evolves into a pronounced double peak further downstream, with the second peak having a slightly lower velocity. A similar pattern is observed in the phase-averaged experimental data, albeit it becomes visible at monitoring points further downstream (i.e., in point 6). Another noteworthy observation regarding the velocity peaks occurs after the gust is generated (i.e., for $t/\Delta t_{\text{gust}} > 1$), specifically at the monitoring points 5 to 9. A third (small) velocity peak is formed in the far wake of the generated gust. This overshoot, similar to the preceding undershoot, becomes more pronounced along the streamwise direction.

Overall, this qualitative comparison shows that the simulation methodology suggested allows to describe the gust generation process in the wind tunnel. In the near future, it is planned to carry out several wind gust simulations with varying initial conditions and then to phase-average the data to allow a direct comparison with the measured data.

5 Conclusions

The objective of the present study was to simulate and analyze discrete wind gusts generated by a recently developed gust generator relying on an adaptive wind tunnel's nozzle. Employing an immersed boundary method with a direct forcing approach

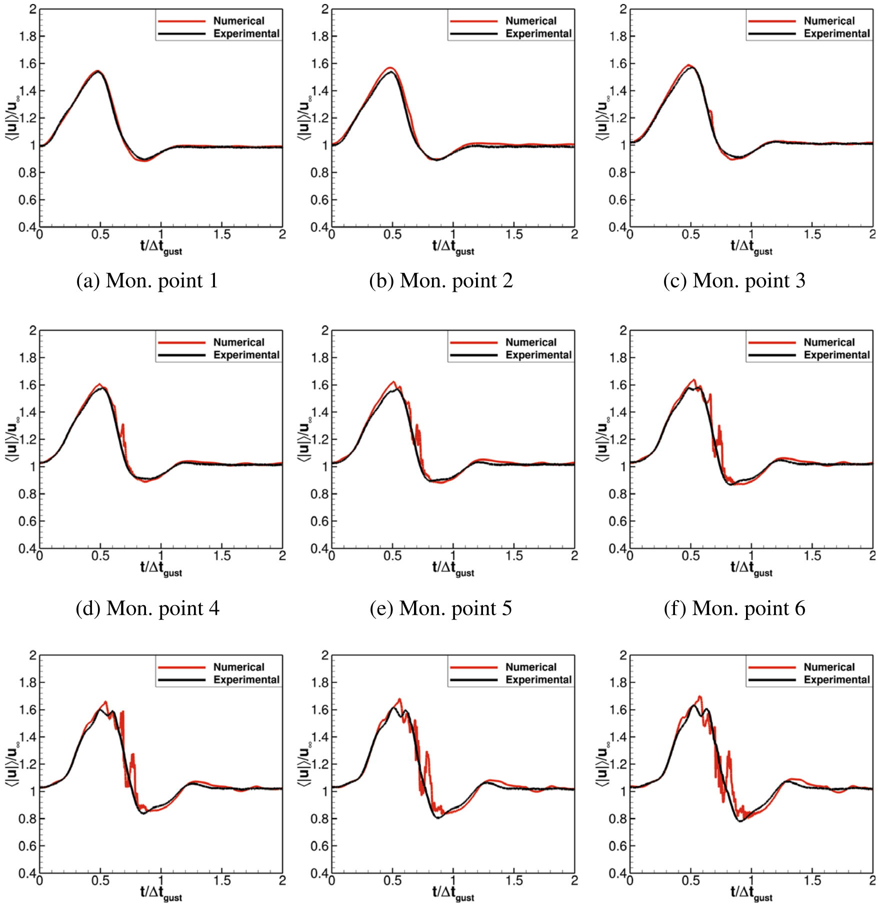

(a) Mon. point 1 (b) Mon. point 2 (c) Mon. point 3

(d) Mon. point 4 (e) Mon. point 5 (f) Mon. point 6

(g) Mon. point 7 (h) Mon. point 8 (i) Mon. point 9

Fig. 7 Time histories of the phase-averaged experimental velocity magnitude [12, 13] and its instantaneous numerical counterpart at the 9 monitoring points depicted in Fig. 6a

to mimic the motion of the upper contour of the nozzle, the challenge was to adjust the methodology for the application on general curvilinear grids. Adopting the moving least square approximation [10] and applying a non-uniform distribution of the Lagrangian markers adjusted to the local Eulerian grid resolution, leads to an efficient and reliable high-fidelity simulation tool for this task. The IBM used in the context of LES guarantees smooth pressure and velocity fields without any numerically induced oscillations.

On the physical side, the newly developed gust generation procedure [12, 13] with the adaptive nozzle leads to a larger undisturbed gust region in the test section compared to the original paddle design [14]. Reasons are the smoother free shear layer and the weaker wall-normal velocities arising in the vicinity of the nozzle's outlet.

A comparison between the phase-averaged experimental data [12, 13] based on 46 individual gusts and the predicted instantaneous velocities at the monitoring points show a high degree of coincidence regarding the maximum velocities occurring and the general temporal course of the velocity signals. Further analyses and comparisons must follow, in particular on the basis of phase-averaged data, which are currently not available due to the considerable computational effort involved.

Acknowledgements Computational resources (HPC cluster HSUper) have been provided by the project hpc.bw, funded by dtec.bw–Digitalization and Technology Research Center of the Bundeswehr. dtec.bw is funded by the European Union–NextGenerationEU.

Competing Interests The authors have no conflicts of interest to declare that are relevant to the content of this chapter.

References

1. Boulbrachene K, Breuer M (2024) A numerical method to mimic an experimental wind gust generator: the immersed boundary gust generator. Phys Fluids 36(1):015146. https://doi.org/10.1063/5.0187787
2. Breuer M, De Nayer G, Münsch M, Gallinger T, Wüchner R (2012) Fluid-structure interaction using a partitioned semi-implicit predictor-corrector coupling scheme for the application of large-eddy simulation. J Fluids Struct 29:107–130. https://doi.org/10.1016/j.jfluidstructs.2011.09.003
3. Durst F, Schäfer M (1996) A parallel block-structured multigrid method for the prediction of incompressible flows. Int J Numer Methods Fluids 22(6):549–565. https://doi.org/10.1002/(SICI)1097-0363(19960330)22:6<549::AID-FLD366>3.0.CO;2-7
4. Mittal R, Iaccarino G (2005) Immersed boundary methods. Annu Rev Fluid Mech 37(1):239–261. https://doi.org/10.1146/annurev.fluid.37.061903.175743
5. Peskin CS (2002) The immersed boundary method. Acta Numer 11:479–517. https://doi.org/10.1017/S0962492902000077
6. Rhie CM, Chow WL (1983) Numerical study of the turbulent flow past an airfoil with trailing-edge separation. AIAA J 21(11):1525–1532. https://doi.org/10.2514/3.8284
7. Sen S, De Nayer G, Breuer M (2017) A fast and robust hybrid method for block-structured mesh deformation with emphasis on FSI-LES applications. Int J Numer Methods Eng 111(3):273–300. https://doi.org/10.1002/nme.5465
8. Smagorinsky J (1963) General circulation experiments with the primitive equations I: the basic experiment. Mon Weather Rev 91(3):99–165. https://doi.org/10.1175/1520-0493(1963)091<0099:GCEWTP>2.3.CO;2
9. Uhlmann M (2005) An immersed boundary method with direct forcing for the simulation of particulate flows. J Comput Phys 209(2):448–476. https://doi.org/10.1016/j.jcp.2005.03.017
10. Vanella M, Balaras E (2009) A moving-least-squares reconstruction for embedded-boundary formulations. J Comput Phys 228(18):6617–6628. https://doi.org/10.1016/j.jcp.2009.06.003
11. Wood JN, Breuer M (2023) The Paddle: a novel procedure for artificial gust generation in a wind tunnel. In: Kähler CJ, Fuchs T, Hain R, Scharnowski S, Ruck B, Leder A (eds) Proceedings der 30. Gala–Fachtagung 'Experimentelle Strömungsmechanik', München, pp 37-1–37-8
12. Wood JN, Breuer M (2024) Artificial wind gust generation based on an adaptive nozzle design. In: Rauh C, Ruck B, Leder A (eds) Proceedings der 31. Gala–Fachtagung 'Experimentelle Strömungsmechanik', Berlin, pp 9-1–9-8

13. Wood JN, Breuer M (2025) Experimental study on a novel wind gust generator based on an adaptive nozzle design. J Wind Eng Ind Aerodyn 261:106080. https://doi.org/10.1016/j.jweia.2025.106080
14. Wood JN, Breuer M, Neumann T (2022) A novel approach for artificially generating horizontal wind gusts based on a movable plate: the Paddle. J Wind Eng Ind Aerodyn 230:105170. https://doi.org/10.1016/j.jweia.2022.105170